Biophysical Journal
Article

Biophysical Society

The Role of Early Bioelectric Signals in the Regeneration of Planarian Anterior/Posterior Polarity

Fallon Durant,[1] Johanna Bischof,[1] Chris Fields,[1] Junji Morokuma,[1] Joshua LaPalme,[1] Alison Hoi,[1] and Michael Levin[1,*]

[1]Allen Discovery Center at Tufts University, Department of Biology, Tufts University, Medford, Massachusetts

ABSTRACT Axial patterning during planarian regeneration relies on a transcriptional circuit that confers distinct positional information on the two ends of an amputated fragment. The earliest known elements of this system begin demarcating differences between anterior and posterior wounds by 6 h postamputation. However, it is still unknown what upstream events break the axial symmetry, allowing a mutual repressor system to establish invariant, distinct biochemical states at the anterior and posterior ends. Here, we show that bioelectric signaling at 3 h is crucial for the formation of proper anterior-posterior polarity in planaria. Briefly manipulating the endogenous bioelectric state by depolarizing the injured tissue during the first 3 h of regeneration alters gene expression by 6 h postamputation and leads to a double-headed phenotype upon regeneration despite confirmed washout of ionophores from tissue. These data reveal a primary functional role for resting membrane potential taking place within the first 3 h after injury and kick-starting the downstream pattern of events that elaborate anatomy over the following 10 days. We propose a simple model of molecular-genetic mechanisms to explain how physiological events taking place immediately after injury regulate the spatial distribution of downstream gene expression and anatomy of regenerating planaria.

INTRODUCTION

Regeneration requires the reconstruction of complex anatomical structures and their appropriate integration with the remaining body via precise control of scaling, position, and organ identity. Planaria are free-living flatworms that have an incredible ability to regenerate missing tissue after damage and amputation despite having a rich set of internal organs, three body axes, and a complex brain and central nervous system (1–4), all of which must be recapitulated each time they regenerate. The process by which each wound blastema in a fragment decides what anatomical structure to form has been the subject of study for over 100 years (5,6). Despite considerable progress on the genetics of stem-cell differentiation and signaling pathways controlling these decisions (7–10), many gaps remain in our understanding of how tissue fragments are able to determine which cell types and body structures are missing and at which locations they need to be recreated (11,12). This general question can be assessed most clearly in planaria by investigating the robust ability of cut fragments to establish proper anterior-posterior (AP) axial polarity (13,14). This process includes three functional endpoints: forming the correct number of heads and tails, creating each one at the correct end with respect to the original orientation of the fragment within the host, and scaling new growth (and remaining soma) appropriately to regain proper overall proportions.

The current molecular models of AP polarity establishment in planaria involve feedback loops between Wnt signaling (15) and other genetic determinants of polarity, such as the ERK signaling pathway (14). Components of the Wnt pathway, *β-catenin* and *wnt1*, both repress head formation and promote tail regeneration at posterior wounds in the regenerating planarian (16–21). Consequently, knockdown of *β-catenin* and *wnt1* both result in the growth of ectopic heads instead of tails. Furthermore, RNAi (RNA interference) knockdown of known inhibitors of the Wnt pathway such as *axin* (22) and *APC-1* (17) induce two-tailed phenotypes.

Interestingly, most components of the Wnt pathway do not show differential expression along the AP axis early during regeneration. *Wnt1*, for example, is expressed at both wounds of a middle fragment (19,21,23) and thus does not explain the differential fate of the two ends. Similarly, Hedgehog

Submitted August 14, 2018, and accepted for publication January 16, 2019.

*Correspondence: michael.levin@tufts.edu

Editor: Stanislav Shvartsman.

https://doi.org/10.1016/j.bpj.2019.01.029

signaling, which may in part regulate posterior-specific induction of *wnt* genes (24), seems to operate along the entire nervous system rather than only posteriorly (24). *Notum*, another inhibitor of the Wnt pathway (25), is the only known gene with an asymmetrical transcriptional response in the first 24 h postamputation (26). *Notum* expression first appears at the anterior blastema 6 h after injury (26) and is required for the establishment of proper polarity (27). Notum has been shown to interact with β-catenin via negative feedback (27), but not much is known about what initially breaks the symmetry of the β-catenin-Wnt amplification loop leading to the early asymmetric expression of *notum* (26) and its subsequent repression of β-catenin (27).

To generate the large-scale AP patterning observed in fragments of planaria, the transcriptional circuits in individual cells need spatial inputs that provide positional cues with respect to the axes of the organism. What might be the input that breaks symmetry for the β-catenin-Wnt amplification loop with respect to the two wounds in a fragment and ensures that the respective ends of the fragment acquire the correct anterior and posterior identities? In other systems, such as left-right axis establishment in vertebrates, upstream physiological signals drive transcriptional cascades that implement positional information; these pathways amplify small biophysical biases to align the differential expression of the earliest genes with the correct geometrical regions in the early embryo (28–30). Here, we investigate the hypothesis that a similar system functions during AP axis specification during planarian regeneration.

One type of biophysical cue is the distribution of cell resting potentials across tissues in vivo, which feed into numerous downstream pathways during regenerative pattern control in a range of model systems (31–33). It is already known that bioelectric states are involved in planarian regenerative patterning (11), mirroring conserved roles for biophysical pathways in organ- and organism-scale patterning in vertebrate and invertebrate models (31–33). Classical gain-of-function experiments by Marsh and Beams (34–36) showed the reset of axial polarity by applying external electric fields to regenerating flatworms (37,38). More recently, imaging of endogenous bioelectric gradients (39–41) and loss-of-function strategies targeting ion channels, pumps, and gap-junction proteins have implicated bioelectrics in planarian cell cycle regulation (42), control of head shape (43), size modulation (44), and stable as well as stochastic outcomes in AP polarity (39,40,45–47). However, it is not known how early the bioelectric signaling acts in this context.

To probe the events upstream of the first known asymmetric gene expression, we tested the hypothesis that the instructive membrane voltage (V_{mem}) differences that have been characterized at 24 h postamputation (39) are in fact established and operative far earlier. We used multiple ionophores to briefly and directly manipulate resting potential in regenerating fragments. Transient alterations of V_{mem}, which are only applied for the first 3 h after amputation, permanently impact subsequent gene expression and anatomical patterning events. We present a computational model of dynamic biophysical signaling that synthesizes the bioelectric and gene expression data to explain how bioelectricity works in concert with biochemical positional information systems to enable robust pattern homeostasis during regeneration. Overall, we show that differences in membrane voltage are detectable very early on during regeneration, before the first known differences in gene expression, and that transient, early disruption of membrane voltage can impact polarity establishment during regeneration. This indicates that physiological changes in membrane potential play an important role in the initial regulatory network that re-establishes polarity after injury in planaria.

MATERIALS AND METHODS

Planarian colony care

A clonal strain of *Dugesia japonica* (*D. japonica*) was kept and maintained in accordance to Oviedo et al. (41), and individuals were starved >7 days before all experiments were performed and continued to be starved for the duration of the experiment. Starvation is necessary to control the metabolic variability seen within individuals (41) and had no effect on regenerative speed or ability. Planaria at the beginning of each experiment were 5–15 mm in length before being amputated into fragments.

Ionophore treatment and amputations

Amputations were performed as in Nogi and Levin (47). Fragments resulting from cuts made immediately posterior to the pharynx and half way between the tail tip (PT fragments) were made using a sharp scalpel and cut on a moistened cooled Kimwipe (Kimberly-Clark, New Milford, CT) and piece of black filter paper. Immediately after cutting, fragments were transferred to either a 0.24 μM nigericin (Adipogen) + 15 mM potassium gluconate (Sigma-Aldrich, St. Louis, MO) solution ("nigericin solution") or a 0.08 μM Monensin (Cayman Chemical, Ann Arbor, MI) + 90 mM sodium gluconate (Sigma-Aldrich) solution ("monensin solution"). All reagents were titered for toxicity. 10 mM nigericin and 7.2 mM monensin stock solutions were made by dissolving either nigericin or monensin in ethanol. Nigericin and monensin working solutions were then made by first dissolving potassium gluconate or sodium gluconate in commercial natural spring water (Poland Spring; Poland Spring Water, Framingham, MA), then adding nigericin or monensin stock to the appropriate concentration in the gluconate solutions. Control solutions contained corresponding amounts of ethanol in water (0.0024 and 0.0011% ethanol solutions, respectively). Nigericin, monensin, and ethanol control solutions were removed 3 h postamputation and the fragments were washed three times in water, and the animals were allowed to regenerate in groups of 30–40 worms at 20°C for the first 7 days after amputation in deep-dish plates (100 × 20 mm; Fisherbrand; Thermo Fisher Scientific, Waltham, MA). Animals were then moved to 10°C to prevent fissioning. Double-headed planaria were imaged 4 weeks postamputation for morphometric analysis.

Evaluation of epidermal cell size

PT fragments were treated in a solution of 0.24 μM nigericin + 15 mM potassium gluconate or in a control solution with 0.0024% ethanol, combined with 300 nM Akita SS44DC dye (stock 1 mg/mL in water; Akita Innovations, North Billerica, MA) for 30 min. This dye efficiently labels cell membranes (48). Fragments were mounted in low-melt agarose, and cells on the

dorsal surface were imaged on a Nikon AZ100M Stereomicroscope (Nikon, Tokyo, Japan). For each worm fragment, the area of 20 cells that had clear boundaries was measured using the "Measure" function in Fiji software. Number of pixels used in the "Measure" function was converted to μm in Fiji. Quantitative data resulting from this analysis are presented in the Supporting Material.

Phenotype scoring and statistical analysis

Scoring was performed using a Zeiss SV6 dissecting microscope (Oberkochen, Germany). Criteria for a double-headed phenotype were at least one eye on each of the anterior and posterior poles. Samples were allowed to regenerate until at least day 14 before scoring. Sample sizes reflected in text are pooled from at least three replicate experiments over the course of several months.

In situ hybridization

Animals were fixed in formaldehyde-based solution for whole-mount in situ hybridization as in Pearson et al. (49) using the probe *D. japonica notum*. The partial codon of *D. japonica notum* (accession number MH000608) was synthesized (GeneArt; Thermo Fisher Scientific) based on the sequence homology from the RNA-seq data used in Chan et al. (50) and was cloned into a vector pCRII-TOPO (Thermo Fisher Scientific). Against this, the in situ probe was generated against the full-length clone and was hydrolyzed to a shorter length for better penetration.

Gene knockdown with RNA interference

Double-stranded RNA (dsRNA) was synthesized as in Rouhana et al. (51) and injected as in Oviedo et al. (52). *D. japonica β-catenin* dsRNA (46) was injected on days 1–3, and worms were cut on day 7 into five pieces as shown in (46). For V_{mem} imaging, animals were imaged in $DiBAC_4(3)$, as below, 3 h postamputation. Double-headed worms were imaged for morphometric analysis 4 weeks postamputation.

Membrane voltage reporter assay

Bis-[1,3-dibarbituric acid]-trimethine oxanol ($DiBAC_4(3)$; Invitrogen, Carlsbad, CA) was used for all membrane voltage-reporting assays as in Adams et al. (53) and Oviedo et al. (41). Planaria were amputated as above to produce PT fragments that were treated in nigericin, monensin, or control ethanol solutions. 3-h-time-point animals were treated in drug with added $DiBAC_4(3)$ immediately after amputation and remained in the same solution for membrane voltage imaging at 3 h postamputation. 6-h-time-point animals were removed as above, washed in water, and placed in a $DiBAC_4(3)$ solution half an hour before imaging. Wild-type, untreated animals used in experiments to describe the timeline of bioelectric signaling within the first 24 h of regeneration were also soaked in a $DiBAC_4(3)$ solution for half an hour before imaging. Planaria were immobilized using 2% low-melting-point agarose and Planarian Immobilization Chips (54). Ethanol-treated controls were imaged side by side on the same chip in tandem with ionophore-treated animals, ventral side up, so that direct comparisons between pairs could be made. Animals were tracked individually in multiwell, nontreated cell culture plates (24 well; Greiner Bio-One, Monroe, NC). Functionality of $DiBAC_4(3)$ was verified recently in (39). Voltage-profiling data are limited to the outermost layer of cells because of the opacity of pigmentation of planarian tissues.

Image collection and processing

Membrane voltage images were collected using a Nikon AZ100M Stereomicroscope (Nikon) with an Andor Technology DL-604M VP camera (South Windsor, CT), using an epifluorescence optics fluorescein isothiocyanate filter (GFP Hard Coat: 470/40, 495, 525/50). Images were pseudocolored using NIS-Elements imaging software (Nikon). Original black and white images were flat-field corrected using the software Fiji (55). All other images were collected using a Nikon SMZ1500 microscope with a Retiga 2000R camera (Qimaging, Surrey, BC, Canada) and Q-Capture imaging software (Qimaging). Adobe Photoshop (Adobe Systems, San Jose, CA) was used to organize figures, rotate and scale images, and improve visibility of entire image with the exception of the membrane voltage images, which were unaltered for brightness.

Statistics and analysis of membrane voltage-reporter assay data

Quantitative comparisons of anterior versus posterior blastemas and ionophore-treated versus control ethanol-treated animals were performed using Fiji (55). To evaluate differences between blastemas, a selection box measuring 15 $\times$ 30 pixels was aligned at the anterior and posterior blastemas, and average intensity was quantified using the "Measure" function. For the ionophore and *β-catenin*-dsRNAi $DiBAC_4(3)$ experiments, the area of each entire fragment was selected, and average intensity was quantified using the "Measure" function. Both analyses were performed in the software after background and flat-field image corrections. Statistical comparisons between anterior and posterior blastemas and between ionophore- and ethanol-treated animals (as well as a control versus control comparison) were made using Microsoft Excel to calculate Student's *t*-test (two-tailed distribution, paired samples, unequal variance). Before running each *t*-test, each data set was verified to be normally distributed using the Shapiro-Wilk test using a $p = 0.01$ threshold. All quantitative data can be found in the Supporting Material.

Morphometric analysis

Worms were relaxed with ice water and imaged using a Nikon SMZ1500 microscope with a Retiga 2000R camera (Surrey, BC, Canada) and Q-Capture imaging software (Surrey, BC, Canada). Landmark data were then recorded using ImageJ (Bethesda, MD) (56). Landmarks were chosen as in Emmons-Bell et al. (43) and included an extra landmark on each side to indicate ridges formed by improper scaling phenotypes or smooth transition from head to body. MorphoJ (Manchester, UK) (57) was used for principal components analysis to quantify and graphically represent changes in scaling morphology. MorphoJ was also used to calculate Procrustes distances and perform statistical analyses.

Predictive modeling

An interactive simulation tool implementing the model of wound blastema response to bioelectric state described below was developed using javascript and HTML Canvas. The wound-response model calculates quantitative head and tail regeneration probabilities for anterior and/or posterior amputations transverse to the AP axis as functions of the bioelectric state of the wound blastema. The simulation tool runs this model for simulated amputation experiments for which the initial bioelectric state of the intact animal, amputation position(s) along the AP axis, bioelectric response to amputation, and external (e.g., drug-induced) modifications of V_{mem} at wound blastema can be manipulated as parameters. This simulation tool can be manipulated and its source code examined at https://chrisfieldsresearch.com/bcar-model.htm.

Chemical analysis of ionophore washout

Worms were flash frozen without any liquid and stored at -80°C until preparation. For preparation for LC/MS analysis, samples were thawed; 3-mm

glass beads (Milipore, Burlington, MA) were added to the tissue before vortexing for 1 min. Ethanol was added as a solvent, and samples were vortexed again. Liquid phase was removed and centrifuged for 20 min at 14,000 rotations per minute at 4°C. The upper clear phase was removed and filtered through a 0.2 μm polytetrafluoroethylene-syringe filter (Whatman, Maidstone, UK). Samples were stored at −80°C before analysis. The standard solution was 1 mM nigericin or monensin in 100% ethanol.

Detection of nigericin and monensin by LC/MS (Harvard Faculty of Arts and Sciences Core Facility, Cambridge, MA) was carried out on a Thermo Scientific Dionex UltiMate 3000 UHPLC (ultra-high performance liquid chromatography) coupled to a Thermo Q Exactive Plus mass spectrometer system (Thermo Fisher Scientific) equipped with an HESI-II electrospray ionization source. Data were acquired with Chromeleon Xpress software for UHPLC and Thermo Xcalibur software version 3.0.63 for mass spectrometry and processed with Thermo Xcalibur Qual Browser software version 4.0.27.19.

A 5-μL sample was injected onto the UHPLC including an HPG-3400RS binary pump with a built-in vacuum degasser (Thermo Fisher Scientific) and a thermostatted WPS-3000TRS high-performance autosampler (Thermo Fisher Scientific). A Symmetry Shield RP18 analytical column (2.1 × 150 mm, 3.5 μm) from Waters (Milford, MA) was used at the flow rate of 0.3 mL/min using 0.2% acetic acid in water as mobile phase A and 0.2% acetic acid in methanol as mobile phase B. The column temperature was maintained at room temperature. The following gradient was applied: 0–2.4 min, 0% B isocratic; 2.4–3.4 min, 0–70% B; 3.4–4.4 min, 70–100% B; 4.4–8.4 min, 100% B isocratic; 8.4–8.5 min, 100–0% B; and 8.5–13.5 min, 0% B isocratic.

The MS conditions were as follows: negative ionization mode for all targets; full scan mass range, m/z 60–850; resolution, 7000; automatic gain control target, 1e6; maximal ionization time, 220 ms; spray voltage, 3500 V; capillary temperature, 280°C; sheath gas, 47.5; auxiliary gas, 11.25; probe heater temperature, 412.5°C; S-Lens radio frequency level, 50.00. A mass window of ±5 ppm was used to extract the ion of $[M\text{-}H]^-$ for all the targets. Targets were considered detected when the mass accuracy was less than 5 ppm and there was a match of isotopic pattern between the observed and the theoretical samples and a match of retention time between those in real samples and standards.

RESULTS

Bioelectric differences between anterior and posterior blastemas are detectable before asymmetric anterior gene expression

Previous work has shown that bioelectric signaling changes along the AP axis of regenerating planaria as early as 24 h after amputation (40), but it was not known how early this difference is established. We used $DiBAC_4(3)$, a voltage-reporting dye, to assay voltage differences between the anterior and posterior blastema as early as 1 h postamputation. Although currently the technology does not permit us to quantitatively determine absolute V_{mem} for planarian cells, we were able to determine relative comparisons of V_{mem} between samples or within the same worm fragment.

Even at the earliest time points assayed (1 h after amputation), regardless of cut location along the AP axis, anterior blastemas were more depolarized than the posterior blastemas of adjacent fragments (Fig. 1 *A*). Similarly, the significant differences between anterior and posterior blastemas on the same fragment seen at 3 h after amputation (Fig. 1 *Ba*, quantified in Fig. 1 *C*) persisted at 6, 12, 18, 24, and 48 h after amputation (Fig. 1 *Bb–d*, quantified in Fig. 1 *C*).

The earliest previously described distinguishing factor between anterior and posterior blastemas in planaria, as determined by RNA sequencing (RNA-seq) profiling, is asymmetric expression of the gene *notum*, which first becomes detectable at 6 h postamputation (26). This early asymmetry is crucial for establishing proper head-tail formation in regenerating *Schmidtea mediterranea (S. mediterranea)*, a closely related planarian species (27). Thus, we hypothesize that *notum* expression follows a similar timeline during head-tail axis establishment in *D. japonica*. To characterize the transcriptional response of *notum* during early regeneration in *D. japonica*, we first identified the *D. japonica* homolog of *notum* and characterized its expression pattern relative to the time course of bioelectric state changes after amputation described above. In situ hybridization for *D. japonica notum* RNA showed a similar expression pattern to that found in *S. mediterranea* (27,58). No expression at either blastema was detectable before or at 3 h postamputation, the time point at which we observed a significant depolarization of the anterior blastema relative to the posterior blastema (Fig. 1 *Da* and *b*). Higher levels of *notum* expression at the anterior blastema as compared to the posterior blastema were observed at 6 h postamputation (Fig. 1 *Dc*). *Notum* expression at 12, 18, and 24 h postamputation also corresponded to what has been previously found in the literature in *S. mediterranea* (27) (Fig. S1 *A*). Although there may be earlier differences in expression of other genes that have yet to be discovered (ones that can function at expression levels below detection even by RNA-seq) and there are possibly other earlier cellular events that may play a role in early axial establishment (including phosphorylation), we conclude that bioelectric asymmetries between the anterior and posterior blastemas occur before the earliest asymmetric gene known to be expressed, *notum*.

Early alteration of bioelectric state results in robust changes to AP polarity

To determine whether the early bioelectric state of planarian tissue is functionally important for proper establishment of AP polarity after regeneration, we sought to directly alter the resting potential of cells. We chose to alter the resting potential via ionophore treatment rather than RNAi against channel and pump proteins to avoid disruption of any potential nonbioelectric roles of channels or pump proteins. We exposed fragments to the potassium ionophore nigericin (59) in combination with potassium gluconate to optimize depolarization of the tissue. Fragments cut posterior to the pharynx and anterior to the tail (PT fragments) were soaked in 0.24 μM nigericin + 15 mM potassium gluconate solution immediately after cutting for 3 h before switching them to water (Fig. 2 *A*). As expected, at 3 h postamputation, nigericin-solution-treated fragments were significantly depolarized compared with fragments treated in control

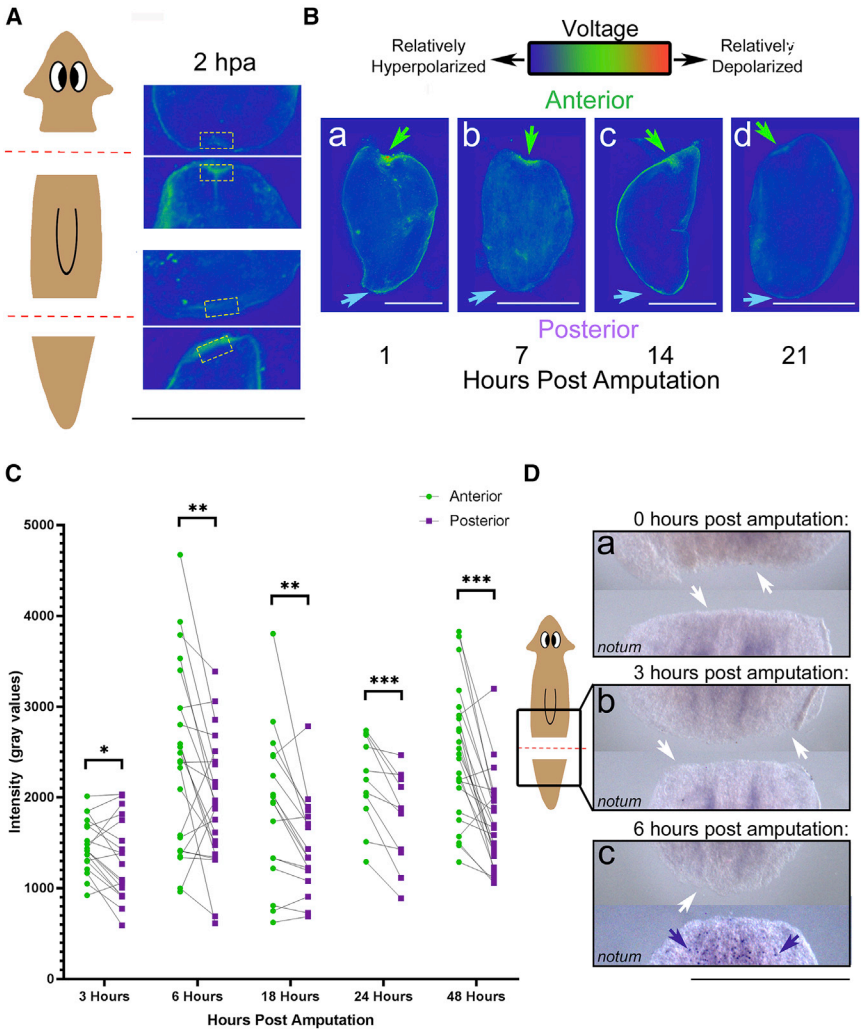

FIGURE 1 AP differences in bioelectric signaling exist before the earliest asymmetrically expressed gene *notum* appears. (*A* and *B*) V_{mem} reporter assay using $DiBAC_4(3)$ is shown. Images are pseudocolored blue-green-red. Brighter pixels (*red*) are most positively charged on the inside of cells relative to the outside, i.e., relatively depolarized. Pixels of lower intensity (*blue*) are relatively hyperpolarized or more negatively charged on the inside of cells relative to the outside. Green arrows indicate anterior blastema, and blue arrows indicate posterior blastema. (*A*) Untreated wild-type (WT) *D. japonica* fragments cut from the same worm 2 h before $DiBAC_4(3)$ imaging are shown. Boxes indicate paired wound sites that were once in the same location in the animal. Anterior-facing blastemas on posterior fragments are significantly depolarized compared with posterior-facing blastemas on anterior fragments, which were located in the same position in the whole worm before amputation ($p < 0.05$, N = 14, paired *t*-test). (*B*) WT fragments in $DiBAC_4(3)$ at (*a*) 1 h, (*b*) 7 h, (*c*) 14 h, and (*d*) 21 h after amputation with anterior blastema oriented toward the top and posterior blastema oriented to the bottom are shown. (*C*) Quantification of $DiBAC_4(3)$ fluorescence intensity at the anterior and posterior blastema of the same individual fragments during regeneration at 3 h (N = 19), 6 h (N = 23), 18 h (N = 17), 24 h (N = 11), and 48 h after cutting (N = 24) is shown. Blastemas from the same fragment are connected by a line. $*p < 0.05$, $**p < 0.01$, $***p < 0.005$, paired *t*-test. (*D*) Timeline indicating *notum* expression in WT regenerating *D. japonica* at (*a*) 0 h, (*b*) 3 h and (*c*) 6 h postamputation, as determined by in situ hybridization, is shown. See Fig. S1 for notum expression at later time points. Amputation plane is indicated in red on the sketch. Each panel representative of a time point includes the posterior wound site of the anterior portion of an amputated worm (*top*) and the anterior wound site of the posterior portion of an amputated worm (*bottom*). Purple arrows indicate punctate expression pattern. White arrows mark the edge of the blastema with no signal. Yellow boxes in (*A*) demarcate regions of interest. Scale bars, 1 mm throughout. To see this figure in color, go online.

solution (0.0024% ethanol in water) (Fig. 2 *Bd*, as compared to Fig. 2 *Ba* and quantified in Fig. 2 *Bg*; alternate quantification in Fig. S2, *A* and *B*). Any potential osmotic effects of incubation in the nigericin solution were tested by measuring the size of cells in the epidermis in nigericin-solution-treated fragments versus control-solution-treated fragments. Consistent with published data showing significant edema and regenerative failures induced by osmotic shock (60,61), we observed no difference in the size of the cells (Fig. S3 *A*, quantified in Fig. S3 *B*), indicating that the difference in osmolarity between the solutions is unlikely to explain the observed phenotype.

The observed depolarization induced by short-term incubation in nigericin solution (Fig. 2 *Bd*, compared to Fig. 2 *Ba*) resulted in the regeneration of double-headed planaria in 13% of observed worms (Fig. 2 *Bf*) compared to 0% in controls (Fig. 2 *Bc*). The remaining 87% of animals regenerating in nigericin solution formed morphologically normal single-headed worms, indistinguishable from controls, with no intermediate phenotypes.

Double-headed planaria were also produced by presoaking animals in potassium gluconate without added nigericin for a week before amputation (8%, N = 60, of regenerated treated worms compared to 0% of regenerated worms in controls), revealing that the induced patterning changes were not due to any secondary effects of nigericin. We hypothesize that presoaking of the animals is required in the absence of ionophore to allow time for high potassium levels in the external medium to propagate past the protective integument and into the interstitial milieu of the animal so as to affect the V_{mem} of deep tissues. Thus, we conclude that patterning of double-headed planaria can result from a transient bioelectric signal that is converted into stable biochemical and anatomical consequences.

We next asked whether the induction of the double-headed state was a specific consequence of nigericin or of changes in

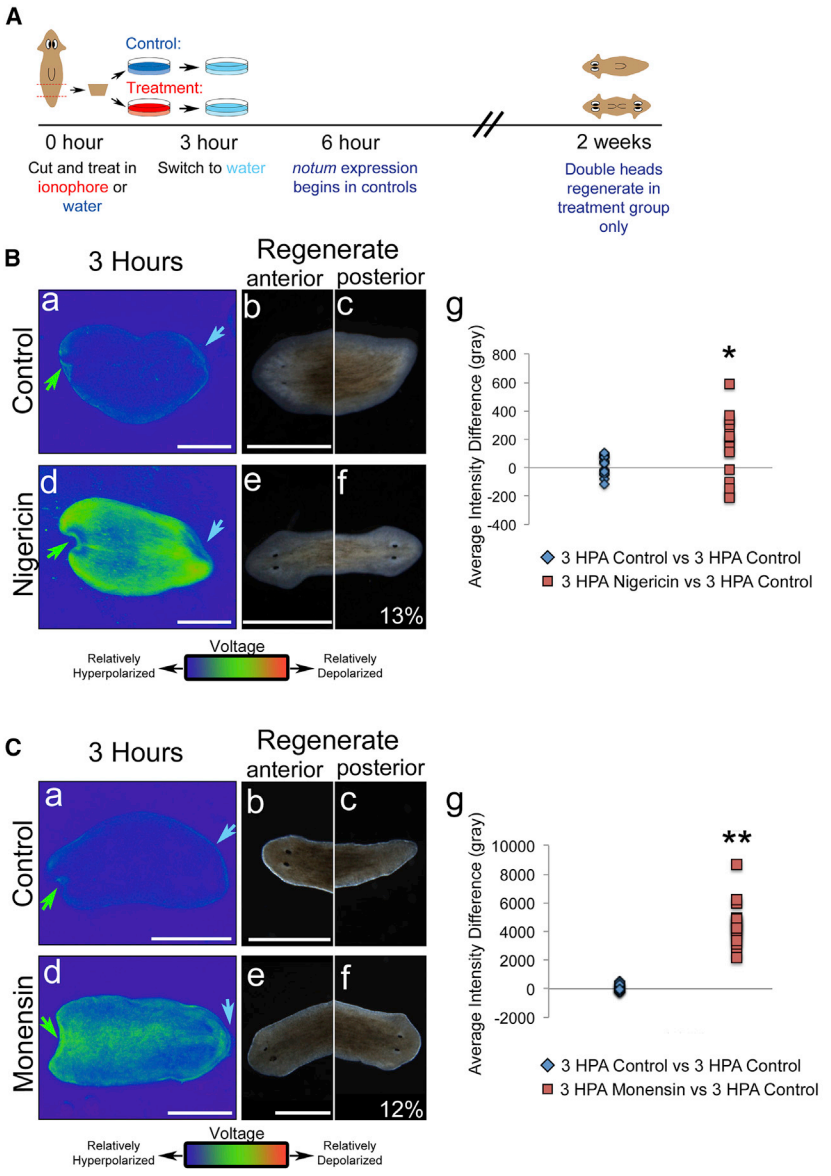

FIGURE 2 Nigericin and monensin treatment depolarizes worm fragments and leads to regeneration of double-headed planaria. (*A*) Treatment timeline for ionophore (nigericin and monensin) solutions is shown. PT fragments were amputated from WT *D. japonica* and treated with 0.24 μM nigericin + 15 mM potassium gluconate or with 0.08 μM monensin + 90 mM sodium gluconate for the first 3 h postamputation side by side with corresponding ethanol in water controls. Animals were moved from treatment solutions into water and washed three times. Worms regenerated for 2 weeks before they were scored. (*B* and *C*) V_{mem} reporter assay using $DiBAC_4(3)$ is shown. Brighter signal indicates relative depolarization, whereas lower intensity indicates relatively hyperpolarized cells. Green arrows indicate anterior blastema, and blue arrows indicate posterior blastema. (*B*) Treatment with nigericin solution is shown. (*a*) A $DiBAC_4(3)$-stained control *D. japonica* PT fragment 3 h postamputation is shown. (*b* and *c*) Regenerative outcome of the control treatment, showing a single-headed worm, with a head at the anterior (*b*) and a tail at the posterior (*c*), is given. (*d*) A $DiBAC_4(3)$-stained *D. japonica* PT fragment 3 h postamputation treated with nigericin solution is given, showing strong depolarization, (*e* and *f*) which results in 13% double-headed regenerative outcomes for worms, with a head both at the anterior (*e*) and the posterior (*f*) in significantly higher numbers than controls in which this phenotype was not observed ($p < 0.01$, N = 132, Fisher's exact test). (*g*) Quantification of the overall average $DiBAC_4(3)$ fluorescence intensity difference of pairs of control fragments (n = 22 pairs) and pairs of one nigericin-treated fragment with a side-by-side control (n = 18 pairs), all 3 h postamputation, is shown. *$p < 0.05$, unpaired *t*-test. (*C*) Treatment with monensin solution is shown. (*a*) A $DiBAC_4(3)$-stained control *D. japonica* PT fragment 3 h postamputation is shown. (*b* and *c*) Regenerative outcome of the control treatment is given, showing a single-headed worm, with a head at the anterior (*b*) and a tail at the posterior (*c*). (*d*) A $DiBAC_4(3)$-stained *D. japonica* PT fragment 3 h postamputation treated with monensin solution is displayed, showing strong depolarization, (*e* and *f*) which results in 12% double-headed regenerative outcomes for worms, with a head both at the anterior (*e*) and the posterior (*f*) in significantly higher numbers than controls in which this phenotype was not observed ($p < 0.01$, N = 89, Fisher's exact test). (*g*) Quantification of the overall average $DiBAC_4(3)$ fluorescence intensity difference of pairs of control fragments (n = 22 pairs) and pairs of one monensin-treated fragment with a side-by-side control (n = 18 pairs), all 3 h postamputation, is shown. **$p < 0.01$, N = 18 each, unpaired *t*-test. Scale bars, 1 mm. To see this figure in color, go online.

V_{mem} in general. To test the ionophore dependency of these treatment outcomes, we treated fragments with the sodium ionophore monensin (62) and sodium gluconate to increase the intracellular sodium levels and thereby depolarize the cells (Fig. 2 *A*). Exposure of fragments to 0.08 μM monensin + 90 mM sodium gluconate for the first 3 h of regeneration resulted in significant depolarization compared to fragments treated in the control solution (0.0011% ethanol in water) (Fig. 2 *Ca* versus Fig. 2 *Cd* and quantified in Fig. 2 *Cg*, alternate quantification in Fig. S2, *A* and *C*). As observed for regeneration in nigericin solution, exposure of fragments to monensin solution also led to regeneration of double-headed worms (12% of treated worms compared to 0% of controls) (Fig. 2 *Cf* as compared to Fig. 2 *Cc*). Because manipulating either the potassium concentration gradient or sodium influx resulted in double-headed worm phenotypes, we conclude that this phenomenon is dependent on depolarization of the tissue regardless of the mechanism that triggers it.

A model integrating planarian bioelectrics and regenerative outcomes

To understand and control regeneration, it is important to derive the rules underlying patterning outcomes as a

function of physiological state. To achieve this, we constructed a quantitative, computational model of AP axis determination in planaria regeneration based on data from the literature and current findings (Fig. 3). An interactive, quantitative simulation tool of the described model is available at https://chrisfieldsresearch.com/bcar-model.htm. Example quantitative predictions using this tool have been included in Tables S1 and S2.

The model assumes that in a normal, regenerating wild-type worm, there is a distribution of V_{mem} across the AP axis such that the worm is more depolarized at the anterior and more hyperpolarized at the posterior (40). Upon amputation, cells that will form the somatic component of the wound blastema are exposed to a local Ca^{2+} spike from cell debris. The model assumes that these cells respond to higher local Ca^{2+} by opening Ca^{2+} channels in a V_{mem}-dependent way, with depolarized cells opening more Ca^{2+} channels and hence undergoing further depolarization, whereas hyperpolarized cells open fewer Ca^{2+} channels and remain hyperpolarized; this assumption is consistent with observations of Ca^{2+} response in both planaria (40,63,64) and other systems (65–67). The net result of this V_{mem}-dependent response to Ca^{2+} release due to wounding is that the AP V_{mem} distribution in the amputated fragment is amplified to approximately replicate the AP V_{mem} distribution of the intact animal. The blastema cells then compare their current V_{mem} state with the nearby non-blastema cells via gap-junction communication. These nearby cells are assumed to be in the interior of the fragment rather than on the surface. Voltage gating and electrophoretic effects mediated by gap-junction communication between adjacent cells allow small-molecule signaling to occur differentially depending on the relative voltage states of the two connected cells (reviewed in (68–70)).

Whether the brain-head pathway or the tail pathway becomes implemented by a wound blastema is quantitatively determined by the depolarization difference between blastema cells (V_B) and their near neighbors in the interior of the fragment (V_{int}), with a large depolarization difference activating the brain-head pathway and a small or negative difference activating the tail pathway (Fig. 3 *A*). Letting $\Delta V = V_B - V_{int}$, the brain-head activation probability is modeled by a sigmoid response function:

$$Prob(\text{Brain/Head}) = \text{Brain/Head Activation} = 1 \Big/ \left(1 + e^{-\alpha\left(\Delta V - V_{exp}\right)}\right)$$

where the adjustable parameter α (default = 0.8) represents the precision of V_{mem} comparisons and the adjustable parameter V_{exp} represents the baseline or "expected" ΔV.

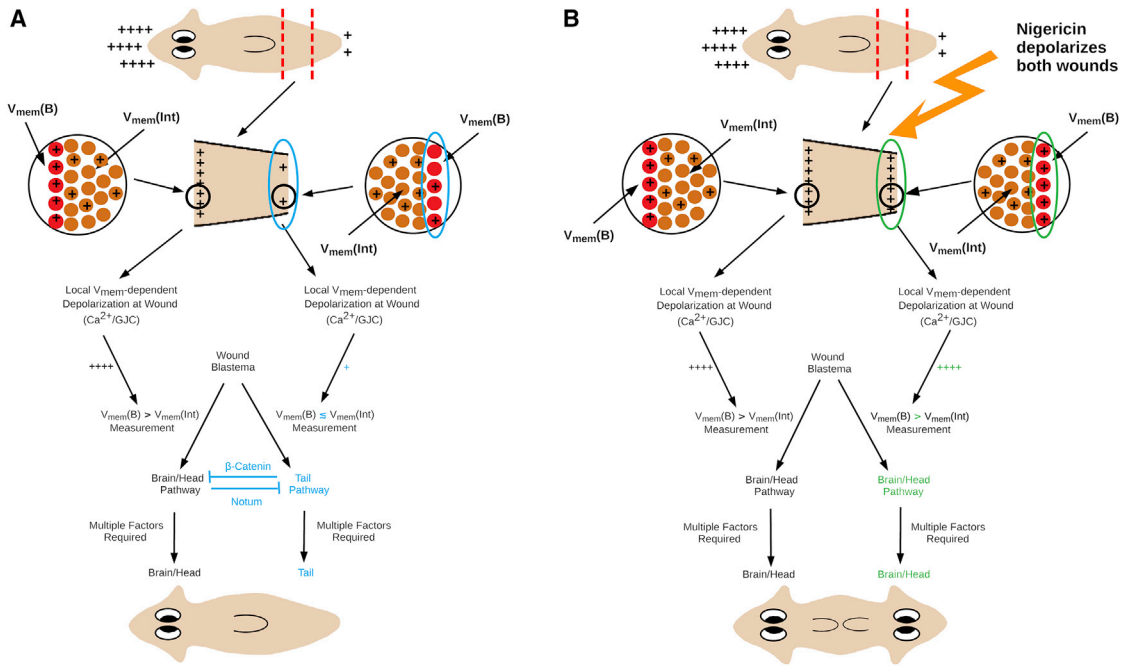

FIGURE 3 A model integrating planarian bioelectrics to regenerative outcomes. (*A*) Cells at the surfaces of wound blastema (inserts) are predicted to measure the difference between their own depolarization (V_{mem}(B)) and the average depolarization (V_{mem}(Int)) of neighboring cells just interior to the wound blastema. If this difference is larger than some threshold value, the brain-head pathway is activated; if the difference is smaller than this threshold or negative, the tail pathway is activated. Branching between pathways is modeled by logistic-function kinetics. Local mutual inhibition by Notum and β-catenin is active in otherwise-untreated WT animals. (*B*) Treatment with nigericin solution (symbolized by *orange lightning bolt arrow*) immediately after amputation depolarizes both wound blastema, leading to brain-head pathway activation and head regeneration at both wounds. Excessive blastema depolarization turns local mutual inhibition by Notum and β-catenin off. To see this figure in color, go online.

The tail activation probability is $1 - Prob$(Brain/Head). The pathway decisions at the two wound blastema depend only on the local depolarization difference ΔV and are completely independent of each other.

Consistent with the observations reported here, activation of the brain-head pathway is assumed to linearly induce *notum* expression at low to intermediate depolarization with sigmoidal saturation at high depolarization; similarly, activation of the tail pathway is assumed to linearly induce *β-catenin* expression (Fig. 3 *A*). Local mutual inhibition by Notum and β-catenin is assumed, in the model, to assure a winner-take-all decision by each blastema to activate either the brain-head or the tail pathway, preventing regenerations in which both head and tail components are regenerated at a single wound blastema; however, this cell-population-level dynamic is not modeled explicitly.

In an ionophore-treated animal, exposed cells at both wounds become similarly depolarized and similarly increase their depolarization in response to increased Ca^{2+} at the wound site, in which case both wound blastemas are more depolarized when they compare their current state with the nonblastema cells (Fig. 3 *B*). This leads to the initiation of the brain-head pathway, although whether the brain-head pathway is fully executed to produce a phenotypically normal brain and head may depend on multiple downstream events.

On a molecular level, a local, concentration-ratio-dependent Notum-β-catenin mutual inhibition is consistent with the previously published tail pathway activation by dsRNAi-mediated knockdown of *notum* at both anterior and posterior wounds and brain-head pathway activation at both wounds enabled by *β-catenin* knockdown (27). Expression of both *notum* and *β-catenin* is predicted to be quantitatively inactivated by excessive blastema depolarization (Fig. 3 *B*). As all cells would be expected to activate the brain-head pathway in a highly depolarized wound blastema, inhibition of the tail pathway by *notum* would not be necessary to prevent tail regeneration in this case. Therefore, we next tested our model's prediction that depolarization induced by nigericin treatment should reduce overall *notum* expression.

Early alteration of V_{mem} changes *notum* expression pattern

Previous work has shown that expression of *notum* is completely absent from the double-headed worms produced by *β-catenin* knockdown (27). Our model suggests that this absence is due to the primary function of *notum* as a means of inhibiting Wnt signaling at anterior wounds rather than a function as a patterning initiator, and because of the presence of a feedback loop (27), the absence of Wnt signaling results in a lack of *notum*. We predicted that in fragments treated with nigericin solution, both blastemas would be heavily depolarized, wiping the physiological asymmetry seen in early regenerating fragments. Our model predicts that in this scenario, the brain-head pathway would activate on each end of the worm and *notum* expression would not occur. We tested this hypothesis by exploring how a 3-h nigericin-solution treatment would affect *notum* expression in regenerating fragments.

As shown above, in a normal regenerating planarian, at 3 h postamputation, the anterior blastema is depolarized relative to the posterior blastema (Fig. 4 *Aa*), whereas *notum* is not expressed anywhere in the fragment (Fig. 4 *Ca*, 100%, N = 20). At 6 h postamputation, the depolarized anterior blastema remains (Fig. 4 *Ab*), and *notum* is expressed asymmetrically at the anterior end of the fragment (Fig. 4 *Cb*, 89%, N = 37). This leads to the regeneration of a worm with normal AP polarity. When a regenerating planarian is exposed to a depolarizing solution of nigericin for the first 3 h of regeneration, at 3 h postamputation, the anterior blastema is depolarized relative to the posterior blastema (Fig. 4 *Ac*, quantified in Fig. 4 *B*), as is observed in controls. However, at 6 h postamputation, unlike controls, the depolarization between the anterior and posterior blastema is indistinguishable (Fig. 4 *Ad*, quantified in Fig. 4 *B*). This occurs even though nigericin is washed out after the first 3 h after amputation and is no longer detectable in the tissue at 6 h (Fig. S4). Nigericin-solution-treated animals similarly do not express notum at the 3-h time point (Fig. 4 *Cc*, 100%, N = 30), but strikingly, correlative with blastema depolarization, *notum* fails to begin its normal expression at 6 h postamputation in a majority of animals (Fig. 4 *Cd*, 85%, N = 27). Given that this same treatment creates ectopic heads, this is consistent with previously published work describing an absence of *notum* expression in the ectopic heads induced by β-catenin RNAi (27). These data collectively suggest that early depolarization disrupts the polarization of the two blastemas, destabilizes the events that lead to AP axis establishment, and leads to an increased rate of regeneration of double-headed worms. We conclude that bioelectric state facilitates expression of *notum* and may influence other downstream targets participating in regenerative control.

AP polarity and scaling are independently regulated by V_{mem} and *β-catenin*

Our model predicts, consistent with the *notum* expression data, that V_{mem} plays an important role in the early regulation of *wnt*-dependent signaling that establishes AP polarity in planaria. To examine possible relationships between these signals, we checked V_{mem} signatures in double-headed animals induced via *β-catenin*-RNAi knockdown (Fig. 5 *A*). A key comparison between *β-catenin*-dsRNAi-induced double-headed worms and those induced by nigericin treatment concerns the scaling of the new tissue relative to the fragment, which is a crucial aspect of regenerative response (6,71–73). Despite the same timeframe of regeneration, the double-headed worms induced by β-catenin inhibition

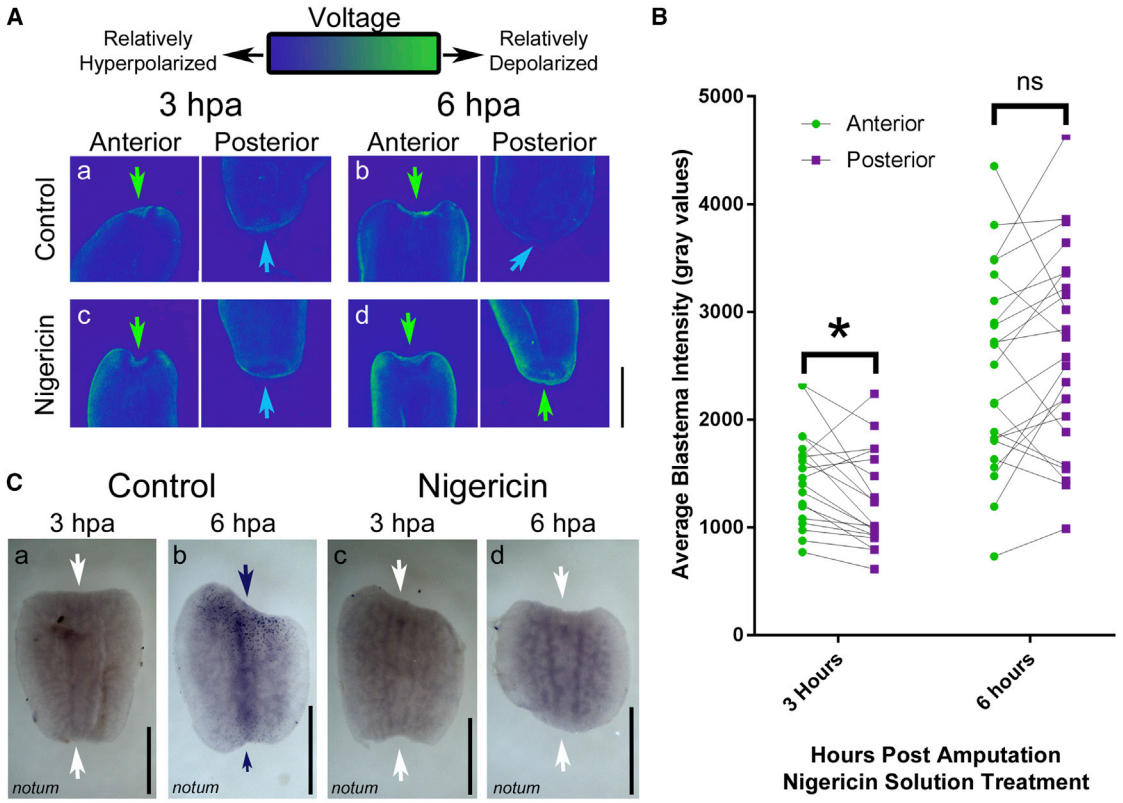

FIGURE 4 A brief, 3-h depolarization changes early expression of *notum*. (*A*) $DiBAC_4(3)$ staining of PT fragments in controls treated for 3 h with ethanol control solutions is shown, imaged at (*a*) 3 h and (*b*) 6 h, focusing on relative intensity distributions at the anterior (*green arrow*) compared to posterior (*blue arrow*) blastema. This is compared to fragments treated for 3 h after amputation in 0.24 μM nigericin + 15 mM potassium gluconate, imaged at (*c*) 3 h and (*d*) 6 h. (*B*) Quantification of the average $DiBAC_4(3)$ fluorescence intensity at the anterior blastema (*green dots*) and posterior blastema (*purple*) in the nigericin-treated fragments at 3 h ($p > 0.5$, N = 19, paired *t*-test) and 6 h ($p < 0.05$, N = 23, paired *t*-test) postamputation is shown. Values for blastemas from the same fragment are connected with a line. *$p < 0.05$, paired *t*-test. (*C*) Timeline of *notum* expression in control treated fragments at (*a*) 3 h and (*b*) 6 h postamputation, as determined by in situ hybridization, is given, showing asymmetric expression of *notum* at the anterior blastema at 6 h. This is compared to absence of *notum* expression in fragments treated with the depolarizing nigericin solution at (*c*) 3 h and (*d*) 6 h postamputation. Purple arrows indicate punctate expression pattern. White arrows mark the edge of the blastema with no signal. Scale bars, 1 mm throughout. To see this figure in color, go online.

were improperly scaled, with newly regenerated heads being well-formed and complete but conspicuously smaller than the original heads and remaining body (Fig. 5 *Ba*). These observations were not seen in nigericin-treated animals (Fig. 5 *Bb*) and could not be rescued by cotreating *β-catenin*-dsRNAi-injected animals with nigericin solution (Fig. 5 *Bc*). This indicates that although V_{mem} regulates AP polarity, *β-catenin* is likely to serve not only AP polarity but also tissue scaling during regeneration because both are disrupted upon its inhibition.

Importantly, we also observed that fragments from worms injected with *β-catenin* dsRNAi did not show a difference in V_{mem} compared to control worms (Fig. 5, *Ca* and *b*) in contrast to the depolarization observed in fragments treated with nigericin solution (Fig. 5 *Cc*, quantified in Fig. 5 *D*), even though both *β-catenin*-dsRNAi and nigericin treatment lead to formation of double-headed worms (Fig. 5 *B*). The fact that *β-catenin* knockdown does not significantly affect bioelectric profiles suggests that β-catenin signaling is not upstream of V_{mem} in this context.

The observation that double-headed worms resulting from nigericin-solution-induced depolarization exhibited heads that were correctly proportioned to the rest of the body was confirmed using quantitative morphometrics. Head morphology differences between *β-catenin*-RNAi animals and nigericin-treated animals were deemed significant (Fig. 5 *E*), whereas combining *β-catenin* dsRNAi with nigericin-solution treatment gave rise to double-headed worms that were quantitatively indistinguishable from those induced by *β-catenin* dsRNAi on its own (Fig. 5 *E*, Procrustes analysis of variance [ANOVA], $p > 0.05$) using the landmarks as defined (Fig. 5 *F*). Thus, depolarization cannot rescue the improper scaling induced by *β-catenin* dsRNAi, suggesting that although V_{mem} depolarization gives rise to correctly scaled heads, it cannot do so if *β-catenin* signaling is disrupted.

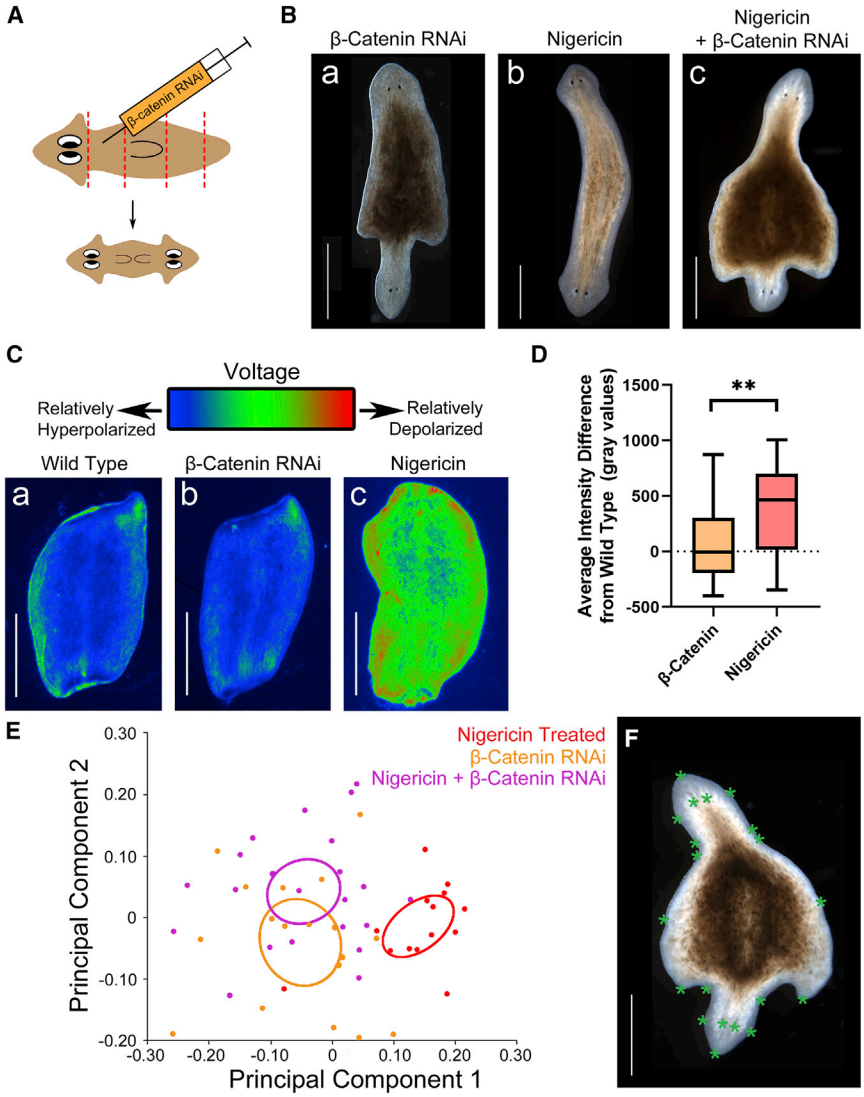

FIGURE 5 *β-catenin* RNAi induces double-headed planaria without depolarization. (*A*) Schematic showing *β-catenin*-dsRNAi injection, which results in regeneration of double-headed planaria from cut fragments, is given. (*B*) (*a*) An example image of a *β-catenin*-dsRNAi-induced double-headed planarian is given, showing abnormal shapes and defects in remodeling toward a normal body shape during the course of regeneration, (*b*) compared to double-headed planaria induced by nigericin treatment and (*c*) one induced by combination of *β-catenin* dsRNAi and nigericin treatment. (*C*) $DiBAC_4(3)$ staining 3 h postamputation of a (*a*) WT fragment and (*b*) a fragment from a *β-catenin*-dsRNAi-injected animal amputated 1 week after injection is given, showing no relative difference in the V_{mem} ($p > 0.05$, paired *t*-test). (*c*) $DiBAC_4(3)$ staining of a fragment treated with nigericin is shown. (*D*) Quantification of the difference between $DiBAC_4(3)$ intensity of *β-catenin*-dsRNAi-injected fragments and their respective controls versus nigericin-treated fragments relative to their respective controls is shown. $^{**}p < 0.01$, paired *t*-test, n = 11. (*E*) Principal component analysis of planarian shape comparing *β-catenin*-RNAi regenerate double-headed planaria (*orange*) versus nigericin-solution-treated regenerate double-headed planaria (*red*) and double-headed planaria induced by nigericin treatment of previously *β-catenin*-RNAi-injected worms (*purple*). Graphical output showing confidence ellipses for means, at a 0.95 probability, of shape data from the three treatment groups (n = 18 *β-catenin* dsRNAi only, n = 22 *β-catenin* dsRNAi + nigericin solution, n = 14 nigericin solution alone) is given. Differences in shape between groups subjected to *β-catenin* dsRNAi and the nigericin-solution-only treatment group were deemed significant with Procrustes ANOVA ($p < 0.0001$). Differences in shape between *β-catenin* dsRNAi and *β-catenin* dsRNAi + nigericin solution were not significant (Procrustes ANOVA, $p > 0.05$). (*F*) An example image of a double-headed worm with landmarks used for shape analysis marked is shown. Scale bars, 1 mm. To see this figure in color, go online.

DISCUSSION

Bioelectric physiology is an important component of repair and regeneration in numerous model systems (32,53,74–81). Endogenous bioelectric fields have been shown to regulate many patterning, morphological, and regenerative processes (32,82–86) and to serve as instructional prepatterns (87,88). In planaria, changes in bioelectric physiology can alter the AP polarity of the worm (40), create changes in head size and shape (43,44), and create stable but stochastic heteromorphoses that appear on subsequent rounds of amputation (39). Here, we show that in normal regenerating planaria, the anterior blastema is depolarized relative to the posterior blastema and that this early depolarization occurs quickly, arising within the first hour after amputation and persisting through 48 h after amputation. This is consistent with an early role for bioelectric signaling in regulating the reformation of polarity because the first known polarized gene expression, that of *notum,* is detectable only after 6 h postamputation. Although there may be earlier cellular events that contribute to axial establishment, such as phosphorylation or asymmetrical transcription of genes that are undetectable by the most sensitive methods currently available, our work indicates that physiological bioelectric signals are observable earlier in the regenerative timeline than any known downstream regulatory networks.

β-catenin has been firmly established as an important regulatory element in the definition of head versus tail identity (16–18,89), and inhibition of *β-catenin* has been long known to create double-headed worms in planaria (17). Our model predicts that V_{mem} lies upstream of regulating AP polarity through *β-catenin,* as confirmed by our observations that *β-catenin* knockdown does not induce differences

in V_{mem} patterns compared to controls. Thus, we propose that depolarization induces changes to β-catenin signaling, which leads to downstream changes in anatomical patterns. The functional data make clear that these physiological signals are important and instructive from the earliest moments of regeneration. Future work testing known transduction mechanisms by which bioelectric state change regulates downstream transcription (31) will address the question of precisely how V_{mem} activates the subsequent genetic targets.

The inability for depolarization to rescue the scaling phenotypes observed with concomitant *β-catenin* RNAi suggests that proper scaling, as observed in depolarization-induced ectopic heads, requires the function of β-catenin. This is not to say that signaling downstream of V_{mem}-dependent changes cannot impact scaling at later time points in a β-catenin-dependent manner, as supported by previous work on the bioelectric determinants of size control (44,90). β-catenin signaling has many inputs and outputs, and it is also possible that compensatory mechanisms later in the regenerative timeline could be reinstating proper scaling in some scenarios. It is an exciting prospect to further explore these potential new roles for β-catenin-dependent scaling and its relationship to V_{mem} alterations in the future.

We developed a model to explain the observed coordination of bioelectric signals with the molecular feedback loops that are important in early AP axis establishment. Our model made the fundamental prediction that expression of *notum* would be inactivated by excessive blastema depolarization such as that seen with nigericin-solution treatments. The lack of *notum* expression in our model is due to all cells activating the brain-head pathway in highly depolarized wound blastemas, predicting that *notum* expression would not be necessary to prevent tail regeneration at anterior blastemas and leading to double-headed planaria. This is consistent with the observed double-headed phenotype and absence of *notum* expression upon knockdown of *β-catenin* (Petersen and Reddien (27)); when the tail pathway-β-catenin signaling is inhibited, *notum* does not need to be expressed so as to limit *β-catenin* expression in the anterior part of the worm. We confirmed this prediction by showing that *notum* was not expressed in early, nigericin-solution-depolarized regenerates. One implication is that the role of asymmetric *notum* expression at the anterior blastema may not be to activate the brain-head pathway, but rather that endogenous levels of depolarization at the anterior blastema are responsible for activating the brain-head pathway, and *notum* serves as a way to maintain the execution of this pathway by inhibiting posterior signaling very early on in regeneration.

Our experiments revealed an interesting temporal aspect of bioelectric change. Consistent with observations in the literature suggesting that both depolarizing agents used in this work, nigericin and monensin, are washable from treated tissue (91–94), we observed that although nigericin and monensin rapidly leave the worms' tissues upon washout, the induced changes in V_{mem} and AP polarity persist. This suggests the existence of a feedback signaling system that allows the maintenance of the depolarized state after the initial trigger is removed. Previous experiments have shown that these maintained, altered bioelectric states have the ability to store altered body plans that stochastically appear upon subsequent rounds of amputation (39). The system maintaining the bioelectric state likely relies on a combination of changes to downstream gene expression or protein modifications (95–97), alterations in gap junctional connectivity, and ion channel states (12,79,98–103). This shows parallels to mechanisms known to drive either intrinsic or synaptic plasticity in the brain, where global modulation of neural networks occurs by modification of voltage-gated ion channels (reviewed in (104)).

Overall, our data reveal that bioelectric signals play an early role in determining polarity in regenerating fragments through the downstream regulatory networks leading to patterned expression of position control genes (24,26). This offers avenues for manipulating large-scale anatomical outcomes in regenerative settings via manipulating membrane potential (81,105), as illustrated here by the induction of double-headed regenerative outcomes through the depolarization of the entire fragment and recently shown in vertebrate models (81).

It is important to note that current tools for detecting changes in V_{mem} can only visualize surface changes in planaria because of strong pigmentation of the epidermis. We anticipate that important events are occurring in deeper tissues. When comprehensive physiomic profiling data become available, it may become possible to extract from the V_{mem} data much more detailed patterning information than merely head-tail instructions. Future work and advances in bioelectric effector methodology and techniques borrowed from the neural decoding field (106,107) will enable probing more deeply into the mechanisms behind cell networks' long-term and dynamic responses to induced changes in V_{mem}.

CONCLUSIONS

Physiological circuits integrate with canonical signaling networks; understanding this interplay is key for a full understanding of the time dependence and complexity of regeneration and for harnessing control over regenerating systems. In planaria, upon injury, the bioelectric state shifts in a polarized manner, establishing an anterior-posterior axis at an extremely early time point. These bioelectric events play an important determinative role in polarity decisions. Future development of optogenetic tools allowing for fine-scale control over V_{mem} patterns will enable this model system to play an important role in decoding the relationship between complex physiological patterns and molecular pathways. Through manipulation of bioelectrical signals,

better control will be gained over the genetic and biochemical cascades that implement morphogenesis of complex structures of correct size and scale. Given that many ion transporter modulators are already approved for clinical use, this knowledge is likely to be beneficial for developing techniques in regenerative medicine.

SUPPORTING MATERIAL

Four figures and two tables are available at http://www.biophysj.org/biophysj/supplemental/S0006-3495(19)30065-7.

AUTHOR CONTRIBUTIONS

F.D. and M.L. designed the experiments and interpreted results. F.D. and J.B. performed and analyzed experimental data. C.F. created the model and wrote the modeling sections of the manuscript. J.M. performed the cloning, the in situ hybridizations, and the dsRNAi injections. J.L. and J.B. assisted with all membrane voltage imaging and drug treatments. A.H. repeated drug treatment experiments, including imaging, and increased number of samples. F.D., M.L., J.B., and C.F. wrote the manuscript with feedback from all authors.

ACKNOWLEDGMENTS

We thank the members of the Levin lab, Alexis Pietak, and many researchers in the planarian regeneration community for useful discussions. We thank Anna Kane and Joshua Finkelstein for their helpful feedback and support in the submission of this manuscript. We are grateful to J. S. Marchant, who provided animals for this study. We also thank Hans Gonzembach and the diligent undergraduates including Hannah Stowe, Quynh Anh Phan, Si Kun Wang, Sara E. Mitchell, Tien Hoang, John Fernandez, and Carolyn H. Nguyen who have helped us tend to our worm colony.

We gratefully acknowledge support by an Allen Discovery Center award from the Paul G. Allen Frontiers Group (No. 12171), the G. Harold and Leila Y. Mathers Charitable Foundation (No. TFU141), the Templeton World Charity Foundation (No. TWCF0089/AB55), and the National Science Foundation (IGERT DGE-1144591).

REFERENCES

1. Cebrià, F. 2008. Organization of the nervous system in the model planarian Schmidtea mediterranea: an immunocytochemical study. *Neurosci. Res.* 61:375–384.
2. Cebrià, F. 2007. Regenerating the central nervous system: how easy for planarians! *Dev. Genes Evol.* 217:733–748.
3. Cebrià, F., T. Kudome, …, K. Agata. 2002. The expression of neural-specific genes reveals the structural and molecular complexity of the planarian central nervous system. *Mech. Dev.* 116:199–204.
4. Cebrià, F., M. Nakazawa, …, K. Agata. 2002. Dissecting planarian central nervous system regeneration by the expression of neural-specific genes. *Dev. Growth Differ.* 44:135–146.
5. Morgan, T. 1898. Experimental studies of the regeneration of Planaria maculata. *Dev. Genes Evol.* 7:364–397.
6. Saló, E., J. F. Abril, …, G. Rodríguez-Esteban. 2009. Planarian regeneration: achievements and future directions after 20 years of research. *Int. J. Dev. Biol.* 53:1317–1327.
7. Rink, J. C. 2013. Stem cell systems and regeneration in planaria. *Dev. Genes Evol.* 223:67–84.
8. Aboobaker, A. A. 2011. Planarian stem cells: a simple paradigm for regeneration. *Trends Cell Biol.* 21:304–311.
9. Reddien, P. W., and A. Sánchez Alvarado. 2004. Fundamentals of planarian regeneration. *Annu. Rev. Cell Dev. Biol.* 20:725–757.
10. Shibata, N., L. Rouhana, and K. Agata. 2010. Cellular and molecular dissection of pluripotent adult somatic stem cells in planarians. *Dev. Growth Differ.* 52:27–41.
11. Durant, F., D. Lobo, …, M. Levin. 2016. Physiological controls of large-scale patterning in planarian regeneration: a molecular and computational perspective on growth and form. *Regeneration (Oxf.).* 3:78–102.
12. Levin, M., A. M. Pietak, and J. Bischof. 2018. Planarian regeneration as a model of anatomical homeostasis: recent progress in biophysical and computational approaches. *Semin. Cell Dev. Biol* Published online April 30, 2018. https://doi.org/10.1016/j.semcdb.2018.04.003.
13. Owlarn, S., and K. Bartscherer. 2016. Go ahead, grow a head! A planarian's guide to anterior regeneration. *Regeneration (Oxf.).* 3:139–155.
14. Umesono, Y., J. Tasaki, …, K. Agata. 2013. The molecular logic for planarian regeneration along the anterior-posterior axis. *Nature.* 500:73–76.
15. Petersen, C. P., and P. W. Reddien. 2009. Wnt signaling and the polarity of the primary body axis. *Cell.* 139:1056–1068.
16. Petersen, C. P., and P. W. Reddien. 2008. Smed-betacatenin-1 is required for anteroposterior blastema polarity in planarian regeneration. *Science.* 319:327–330.
17. Gurley, K. A., J. C. Rink, and A. Sánchez Alvarado. 2008. β-catenin defines head versus tail identity during planarian regeneration and homeostasis. *Science.* 319:323–327.
18. Iglesias, M., J. L. Gomez-Skarmeta, …, T. Adell. 2008. Silencing of Smed-betacatenin1 generates radial-like hypercephalized planarians. *Development.* 135:1215–1221.
19. Petersen, C. P., and P. W. Reddien. 2009. A wound-induced Wnt expression program controls planarian regeneration polarity. *Proc. Natl. Acad. Sci. USA.* 106:17061–17066.
20. Adell, T., E. Salò, …, K. Bartscherer. 2009. Smed-Evi/Wntless is required for β-catenin-dependent and -independent processes during planarian regeneration. *Development.* 136:905–910.
21. Gurley, K. A., S. A. Elliott, …, A. Sánchez Alvarado. 2010. Expression of secreted Wnt pathway components reveals unexpected complexity of the planarian amputation response. *Dev. Biol.* 347:24–39.
22. Iglesias, M., M. Almuedo-Castillo, …, E. Saló. 2011. Early planarian brain regeneration is independent of blastema polarity mediated by the Wnt/β-catenin pathway. *Dev. Biol.* 358:68–78.
23. Rink, J. C., K. A. Gurley, …, A. S. Alvarado. 2009. Planarian Hh signaling regulates regeneration polarity and links Hh pathway evolution to cilia. *Science.* 326:1406–1410.
24. Yazawa, S., Y. Umesono, …, K. Agata. 2009. Planarian hedgehog/patched establishes anterior-posterior polarity by regulating Wnt signaling. *Proc. Natl. Acad. Sci. USA.* 106:22329–22334.
25. Gerlitz, O., and K. Basler. 2002. Wingful, an extracellular feedback inhibitor of Wingless. *Genes Dev.* 16:1055–1059.
26. Wurtzel, O., L. E. Cote, …, P. W. Reddien. 2015. A generic and cell-type-specific wound response precedes regeneration in planarians. *Dev. Cell.* 35:632–645.
27. Petersen, C. P., and P. W. Reddien. 2011. Polarized notum activation at wounds inhibits Wnt function to promote planarian head regeneration. *Science.* 332:852–855.
28. Levin, M. 2006. Is the early left-right axis like a plant, a kidney, or a neuron? The integration of physiological signals in embryonic asymmetry. *Birth Defects Res. C Embryo Today.* 78:191–223.
29. Adams, D. S., K. R. Robinson, …, M. Levin. 2006. Early, H+-V-ATPase-dependent proton flux is necessary for consistent left-right patterning of non-mammalian vertebrates. *Development.* 133:1657–1671.

30. Levin, M., T. Thorlin, …, M. Mercola. 2002. Asymmetries in H+/K+-ATPase and cell membrane potentials comprise a very early step in left-right patterning. *Cell.* 111:77–89.
31. Levin, M., G. Pezzulo, and J. M. Finkelstein. 2017. Endogenous bioelectric signaling networks: exploiting voltage gradients for control of growth and form. *Annu. Rev. Biomed. Eng.* 19:353–387.
32. McLaughlin, K. A., and M. Levin. 2018. Bioelectric signaling in regeneration: mechanisms of ionic controls of growth and form. *Dev. Biol.* 433:177–189.
33. Bates, E. 2015. Ion channels in development and cancer. *Annu. Rev. Cell Dev. Biol.* 31:231–247.
34. Hyman, L. H. 1932. Studies on the correlation between metabolic gradients, electrical gradients, and galvanotaxis. II. Galvanotaxis of the brown hydra and some non-fissioning planarians. *Physiol. Zool.* 5:185–190.
35. Bonaventure, N. 1957. Galvanotropisme de régénérats monstrueux de Planaires: monstres bifides et hétéromorphoses. *C. R. Seances Soc. Biol. Fil.* 151:598–602.
36. Lange, C. S., and V. E. Steele. 1978. The mechanism of anterior-posterior polarity control in planarians. *Differentiation.* 11:1–12.
37. Marsh, G., and H. W. Beams. 1952. Electrical control of morphogenesis in regenerating Dugesia tigrina. I. Relation of axial polarity to field strength. *J. Cell. Comp. Physiol.* 39:191–213.
38. Dimmitt, J., and G. Marsh. 1952. Electrical control of morphogenesis in regenerating Dugesia tigrina. II. Potential gradient vs. current density as control factors. *J. Cell. Comp. Physiol.* 40:11–23.
39. Durant, F., J. Morokuma, …, M. Levin. 2017. Long-term, stochastic editing of regenerative anatomy via targeting endogenous bioelectric gradients. *Biophys. J.* 112:2231–2243.
40. Beane, W. S., J. Morokuma, …, M. Levin. 2011. A chemical genetics approach reveals H,K-ATPase-mediated membrane voltage is required for planarian head regeneration. *Chem. Biol.* 18:77–89.
41. Oviedo, N. J., C. L. Nicolas, …, M. Levin. 2008. Live imaging of planarian membrane potential using DiBAC4(3). *CSH Protoc.* 2008:pdb.prot5055.
42. Barghouth, P. G., M. Thiruvalluvan, and N. J. Oviedo. 2015. Bioelectrical regulation of cell cycle and the planarian model system. *Biochim. Biophys. Acta.* 1848:2629–2637.
43. Emmons-Bell, M., F. Durant, …, M. Levin. 2015. Gap junctional blockade stochastically induces different species-specific head anatomies in genetically wild-type Girardia dorotocephala flatworms. *Int. J. Mol. Sci.* 16:27865–27896.
44. Beane, W. S., J. Morokuma, …, M. Levin. 2013. Bioelectric signaling regulates head and organ size during planarian regeneration. *Development.* 140:313–322.
45. Levin, M. 2014. Endogenous bioelectrical networks store non-genetic patterning information during development and regeneration. *J. Physiol.* 592:2295–2305.
46. Oviedo, N. J., J. Morokuma, …, M. Levin. 2010. Long-range neural and gap junction protein-mediated cues control polarity during planarian regeneration. *Dev. Biol.* 339:188–199.
47. Nogi, T., and M. Levin. 2005. Characterization of innexin gene expression and functional roles of gap-junctional communication in planarian regeneration. *Dev. Biol.* 287:314–335.
48. Bardon, K. M., S. Selfridge, …, L. Takiff. 2018. Synthesis of water-soluble far-red-emitting amphiphilic BODIPY dyes. *ACS Omega.* 3:13195–13199.
49. Pearson, B. J., G. T. Eisenhoffer, …, A. Sánchez Alvarado. 2009. Formaldehyde-based whole-mount in situ hybridization method for planarians. *Dev. Dyn.* 238:443–450.
50. Chan, J. D., D. Zhang, …, J. S. Marchant. 2016. Dataset for a *Dugesia japonica* de novo transcriptome assembly, utilized for defining the voltage-gated like ion channel superfamily. *Data Brief.* 9:1044–1047.
51. Rouhana, L., J. A. Weiss, …, P. A. Newmark. 2013. RNA interference by feeding in vitro-synthesized double-stranded RNA to planarians: methodology and dynamics. *Dev. Dyn.* 242:718–730.
52. Oviedo, N. J., C. L. Nicolas, …, M. Levin. 2008. Gene knockdown in planarians using RNA interference. *CSH Protoc.* 2008:pdb.prot5054.
53. Adams, D. S., A. Masi, and M. Levin. 2007. H+ pump-dependent changes in membrane voltage are an early mechanism necessary and sufficient to induce Xenopus tail regeneration. *Development.* 134:1323–1335.
54. Dexter, J. P., M. B. Tamme, …, E. M. Collins. 2014. On-chip immobilization of planarians for in vivo imaging. *Sci. Rep.* 4:6388.
55. Schindelin, J., I. Arganda-Carreras, …, A. Cardona. 2012. Fiji: an open-source platform for biological-image analysis. *Nat. Methods.* 9:676–682.
56. Schneider, C. A., W. S. Rasband, and K. W. Eliceiri. 2012. NIH Image to ImageJ: 25 years of image analysis. *Nat. Methods.* 9:671–675.
57. Klingenberg, C. P. 2011. MorphoJ: an integrated software package for geometric morphometrics. *Mol. Ecol. Resour.* 11:353–357.
58. Roberts-Galbraith, R. H., and P. A. Newmark. 2013. Follistatin antagonizes activin signaling and acts with notum to direct planarian head regeneration. *Proc. Natl. Acad. Sci. USA.* 110:1363–1368.
59. Harold, F. M., K. H. Altendorf, and H. Hirata. 1974. Probing membrane transport mechanisms with inophores. *Ann. N. Y. Acad. Sci.* 235:149–160.
60. Rink, J. C., H. T. Vu, and A. Sánchez Alvarado. 2011. The maintenance and regeneration of the planarian excretory system are regulated by EGFR signaling. *Development.* 138:3769–3780.
61. Hwang, B., Y. An, K. Agata, and Y. Umesono. 2015. Two distinct roles of the *yorkie/yap* gene during homeostasis in the planarian *Dugesia japonica*. *Dev. Growth Differ.* 57:209–217.
62. Mollenhauer, H. H., D. J. Morré, and L. D. Rowe. 1990. Alteration of intracellular traffic by monensin; mechanism, specificity and relationship to toxicity. *Biochim. Biophys. Acta.* 1031:225–246.
63. Chan, J. D., D. Zhang, …, J. S. Marchant. 2017. Utilizing the planarian voltage-gated ion channel transcriptome to resolve a role for a Ca2+ channel in neuromuscular function and regeneration. *Biochim. Biophys. Acta Mol. Cell Res.* 1864:1036–1045.
64. Chan, J. D., P. N. Agbedanu, …, J. S. Marchant. 2014. 'Death and axes': unexpected Ca^{2+} entry phenologs predict new anti-schistosomal agents. *PLoS Pathog.* 10:e1003942.
65. Barish, M. E. 1983. A transient calcium-dependent chloride current in the immature Xenopus oocyte. *J. Physiol.* 342:309–325.
66. Carl, A., H. K. Lee, and K. M. Sanders. 1996. Regulation of ion channels in smooth muscles by calcium. *Am. J. Physiol.* 271:C9–C34.
67. Ward, J. M., Z. M. Pei, and J. I. Schroeder. 1995. Roles of ion channels in initiation of signal transduction in higher plants. *Plant Cell.* 7:833–844.
68. Mathews, J., and M. Levin. 2017. Gap junctional signaling in pattern regulation: physiological network connectivity instructs growth and form. *Dev. Neurobiol.* 77:643–673.
69. Palacios-Prado, N., S. Sonntag, …, F. F. Bukauskas. 2009. Gating, permselectivity and pH-dependent modulation of channels formed by connexin57, a major connexin of horizontal cells in the mouse retina. *J. Physiol.* 587:3251–3269.
70. Palacios-Prado, N., and F. F. Bukauskas. 2009. Heterotypic gap junction channels as voltage-sensitive valves for intercellular signaling. *Proc. Natl. Acad. Sci. USA.* 106:14855–14860.
71. Oviedo, N. J., P. A. Newmark, and A. Sánchez Alvarado. 2003. Allometric scaling and proportion regulation in the freshwater planarian *Schmidtea mediterranea*. *Dev. Dyn.* 226:326–333.
72. González-Estévez, C., and E. Saló. 2010. Autophagy and apoptosis in planarians. *Apoptosis.* 15:279–292.
73. Potter, C. J., and T. Xu. 2001. Mechanisms of size control. *Curr. Opin. Genet. Dev.* 11:279–286.
74. Kucerova, R., P. Walczysko, …, J. M. Collinson. 2011. The role of electrical signals in murine corneal wound re-epithelialization. *J. Cell. Physiol.* 226:1544–1553.

75. Sebastian, A., S. A. Iqbal, …, A. Bayat. 2015. Electrical stimulation enhances epidermal proliferation in human cutaneous wounds by modulating p53-SIVA1 interaction. *J. Invest. Dermatol.* 135:1166–1174.

76. Zhang, W., and M. Bei. 2015. Kcnh2 and Kcnj8 interactively regulate skin wound healing and regeneration. *Wound Repair Regen.* 23: 797–806.

77. Monteiro, J., R. Aires, …, J. Rodríguez-León. 2014. V-ATPase proton pumping activity is required for adult zebrafish appendage regeneration. *PLoS One.* 9:e92594.

78. Adams, D. S., A. S. Tseng, and M. Levin. 2013. Light-activation of the archaerhodopsin H(+)-pump reverses age-dependent loss of vertebrate regeneration: sparking system-level controls in vivo. *Biol. Open.* 2:306–313.

79. Pietak, A., and M. Levin. 2018. Bioelectrical control of positional information in development and regeneration: a review of conceptual and computational advances. *Prog. Biophys. Mol. Biol.* 137:52–68.

80. Mathews, J., and M. Levin. 2018. The body electric 2.0: recent advances in developmental bioelectricity for regenerative and synthetic bioengineering. *Curr. Opin. Biotechnol.* 52:134–144.

81. Pai, V. P., A. Pietak, …, M. Levin. 2018. HCN2 rescues brain defects by enforcing endogenous voltage pre-patterns. *Nat. Commun.* 9:998.

82. Ardissone, A., V. Sansone, …, I. Moroni. 2017. Intrafamilial phenotypic variability in Andersen-Tawil syndrome: a diagnostic challenge in a potentially treatable condition. *Neuromuscul. Disord.* 27: 294–297.

83. Levin, M., and C. J. Martyniuk. 2018. The bioelectric code: an ancient computational medium for dynamic control of growth and form. *Biosystems.* 164:76–93.

84. Adams, D. S., S. G. Uzel, …, M. Levin. 2016. Bioelectric signalling via potassium channels: a mechanism for craniofacial dysmorphogenesis in KCNJ2-associated Andersen-Tawil Syndrome. *J. Physiol.* 594:3245–3270.

85. Masotti, A., P. Uva, …, B. Dallapiccola. 2015. Keppen-Lubinsky syndrome is caused by mutations in the inwardly rectifying K+ channel encoded by KCNJ6. *Am. J. Hum. Genet.* 96:295–300.

86. Kortüm, F., V. Caputo, …, K. Kutsche. 2015. Mutations in KCNH1 and ATP6V1B2 cause Zimmermann-Laband syndrome. *Nat. Genet.* 47:661–667.

87. Vandenberg, L. N., R. D. Morrie, and D. S. Adams. 2011. V-ATPase-dependent ectodermal voltage and pH regionalization are required for craniofacial morphogenesis. *Dev. Dyn.* 240:1889–1904.

88. Shi, R., and R. B. Borgens. 1995. Three-dimensional gradients of voltage during development of the nervous system as invisible coordinates for the establishment of embryonic pattern. *Dev. Dyn.* 202:101–114.

89. Meinhardt, H. 2009. Beta-catenin and axis formation in planarians. *BioEssays.* 31:5–9.

90. Perathoner, S., J. M. Daane, …, M. P. Harris. 2014. Bioelectric signaling regulates size in zebrafish fins. *PLoS Genet.* 10:e1004080.

91. Budunova, I. V., and L. A. Mittelman. 1992. The effect of K+/H+ antiporter nigericin on gap junction permeability. *Cell Biol. Toxicol.* 8:63–73.

92. Daniele, R. P., S. K. Holian, and P. C. Nowell. 1978. A potassium ionophore (Nigericin) inhibits stimulation of human lymphocytes by mitogens. *J. Exp. Med.* 147:571–581.

93. Pal, R., R. C. Gallo, and M. G. Sarngadharan. 1988. Processing of the structural proteins of human immunodeficiency virus type 1 in the presence of monensin and cerulenin. *Proc. Natl. Acad. Sci. USA.* 85:9283–9286.

94. Brock, T. A., and J. B. Smith. 1982. Reversible stimulation of the Na+/K+ pump by monensin in cultures of vascular smooth muscle. *Life Sci.* 31:1043–1050.

95. Zhang, W., and B. C. Kone. 2002. NF-kappaB inhibits transcription of the H(+)-K(+)-ATPase α(2)-subunit gene: role of histone deacetylases. *Am. J. Physiol. Renal Physiol.* 283:F904–F911.

96. Yang, S. J., H. L. Liang, …, M. T. Wong-Riley. 2004. Ultrastructural study of depolarization-induced translocation of NRF-2 transcription factor in cultured rat visual cortical neurons. *Eur. J. Neurosci.* 19:1153–1162.

97. Levin, M. 2007. Large-scale biophysics: ion flows and regeneration. *Trends Cell Biol.* 17:261–270.

98. Law, R., and M. Levin. 2015. Bioelectric memory: modeling resting potential bistability in amphibian embryos and mammalian cells. *Theor. Biol. Med. Model.* 12:22.

99. Cervera, J., A. Pietak, …, S. Mafe. 2018. Bioelectrical coupling in multicellular domains regulated by gap junctions: a conceptual approach. *Bioelectrochemistry.* 123:45–61.

100. Gallaher, J., M. Bier, and J. S. van Heukelom. 2010. First order phase transition and hysteresis in a cell's maintenance of the membrane potential–An essential role for the inward potassium rectifiers. *Biosystems.* 101:149–155.

101. Cervera, J., A. Alcaraz, and S. Mafe. 2014. Membrane potential bistability in nonexcitable cells as described by inward and outward voltage-gated ion channels. *J. Phys. Chem. B.* 118:12444–12450.

102. van Mil, H., J. Siegenbeek van Heukelom, and M. Bier. 2003. A bistable membrane potential at low extracellular potassium concentration. *Biophys. Chem.* 106:15–21.

103. Williams, S. R., S. R. Christensen, …, M. Häusser. 2002. Membrane potential bistability is controlled by the hyperpolarization-activated current I(H) in rat cerebellar Purkinje neurons in vitro. *J. Physiol.* 539:469–483.

104. Zhang, W., and D. J. Linden. 2003. The other side of the engram: experience-driven changes in neuronal intrinsic excitability. *Nat. Rev. Neurosci.* 4:885–900.

105. Herrera-Rincon, C., V. P. Pai, …, M. Levin. 2017. The brain is required for normal muscle and nerve patterning during early Xenopus development. *Nat. Commun.* 8:587.

106. Oizumi, M., S. Amari, …, N. Tsuchiya. 2016. Measuring integrated information from the decoding perspective. *PLoS Comput. Biol.* 12:e1004654.

107. Tsien, J. Z., M. Li, …, H. Kuang. 2013. On initial brain activity mapping of episodic and semantic memory code in the hippocampus. *Neurobiol. Learn. Mem.* 105:200–210.

Biophysical Journal, Volume *116*

Supplemental Information

The Role of Early Bioelectric Signals in the Regeneration of Planarian Anterior/Posterior Polarity

Fallon Durant, Johanna Bischof, Chris Fields, Junji Morokuma, Joshua LaPalme, Alison Hoi, and Michael Levin

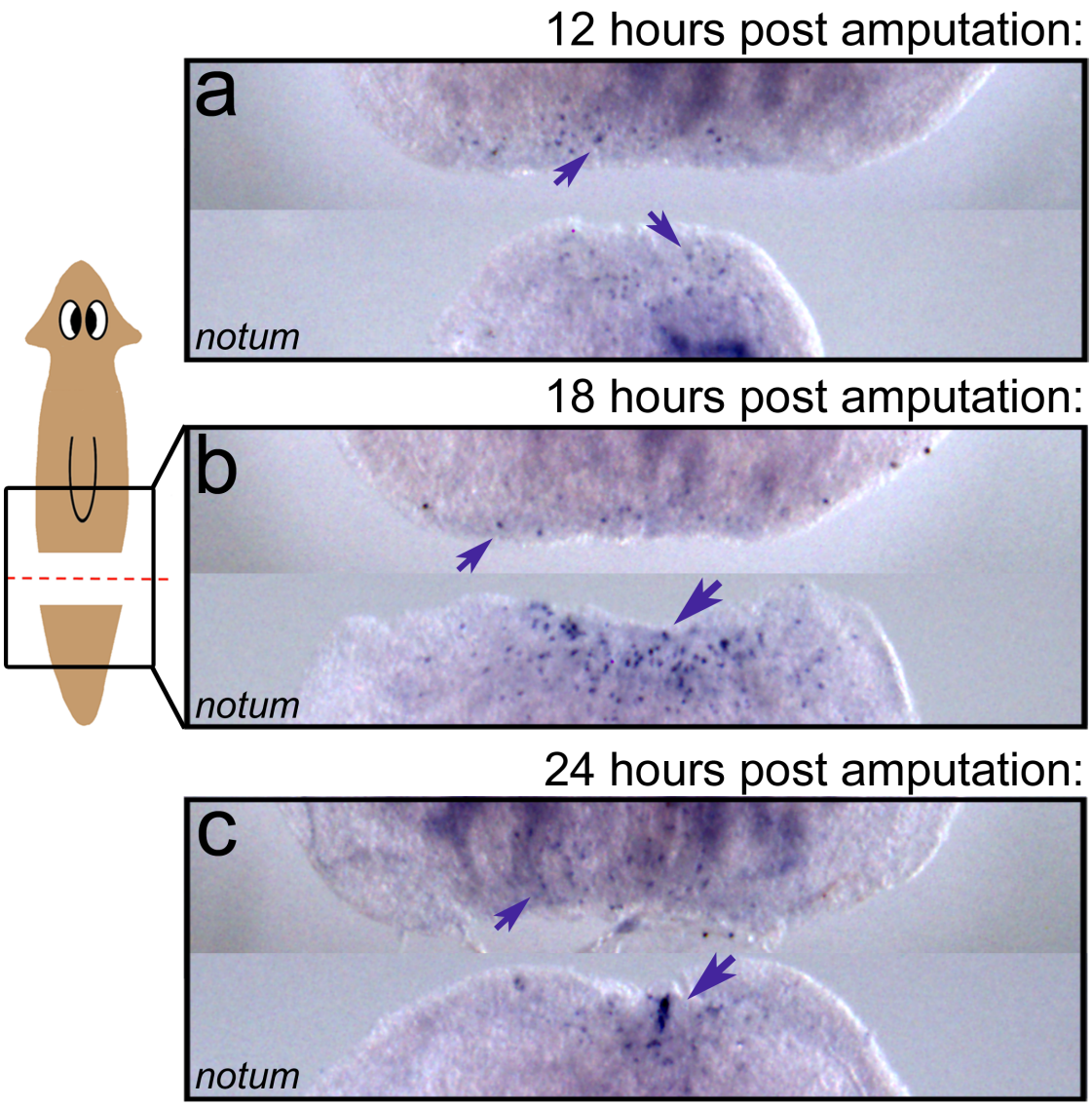

Supplemental Figure 1. *Notum* expression at later timepoints of regeneration. Timeline indicating *notum* expression in WT regenerating DJ at (a) 12 hours, (b) 18 hours and (c) 24 hours post-amputation, as determined by *in situ* hybridization. Amputation plane indicated in red on the sketch. Each panel representative of a timepoint includes the posterior wound site of the anterior portion of an amputated worm (top) and the anterior wound site of the posterior portion of an amputated worm (bottom). Purple arrows indicate punctate expression pattern. Scale bars represent 1 mm throughout.

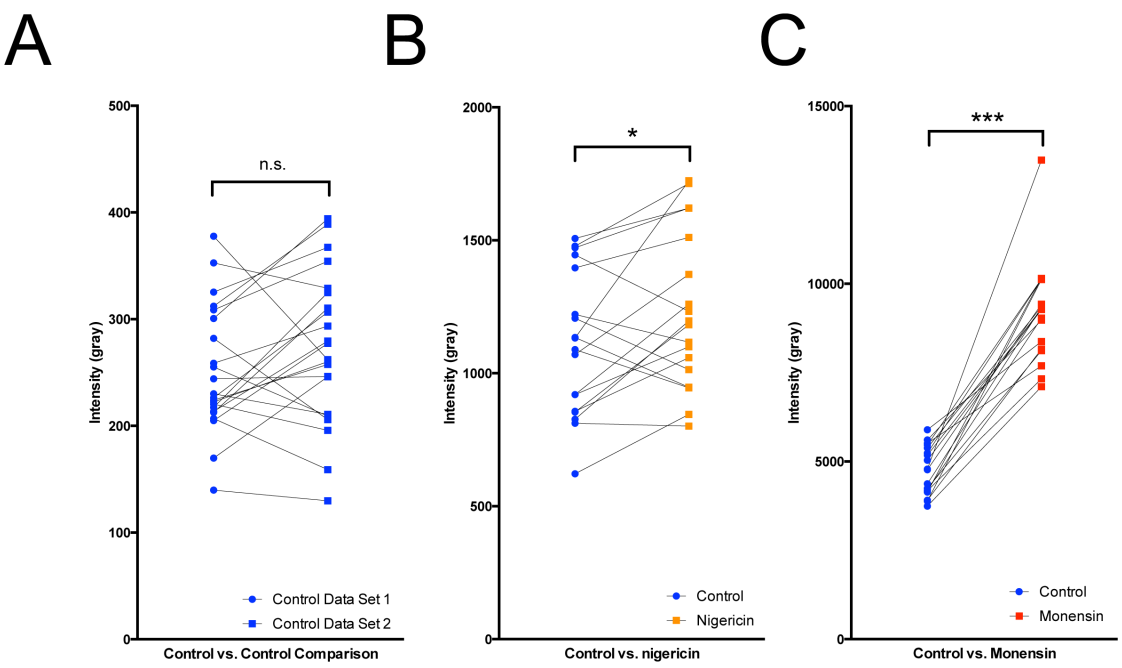

Supplemental Figure 2. Alternate quantification of Figure 2Bg and 2Cg. Re-quantification of the data used in Figures 2Bg and 2Cg, now directly comparing pairs of worm fragments imaged on the same platform. Data indicates overall average $DiBAC_4(3)$ fluorescence intensity of pairs of (A) two control fragments (n=22 pairs, blue, $p>0.05$, paired t-test), (B) pairs of one nigericin-treated fragment (orange) with a side-by-side control (n=18 pairs), and (C) pairs of one monensin-treated fragment (red) with a side-by-side control (n=18 pairs) all 3 hours post amputation. Paired samples are indicated with a line. n.s.: not significant, * $p<0.05$, *** $p<0.001$.

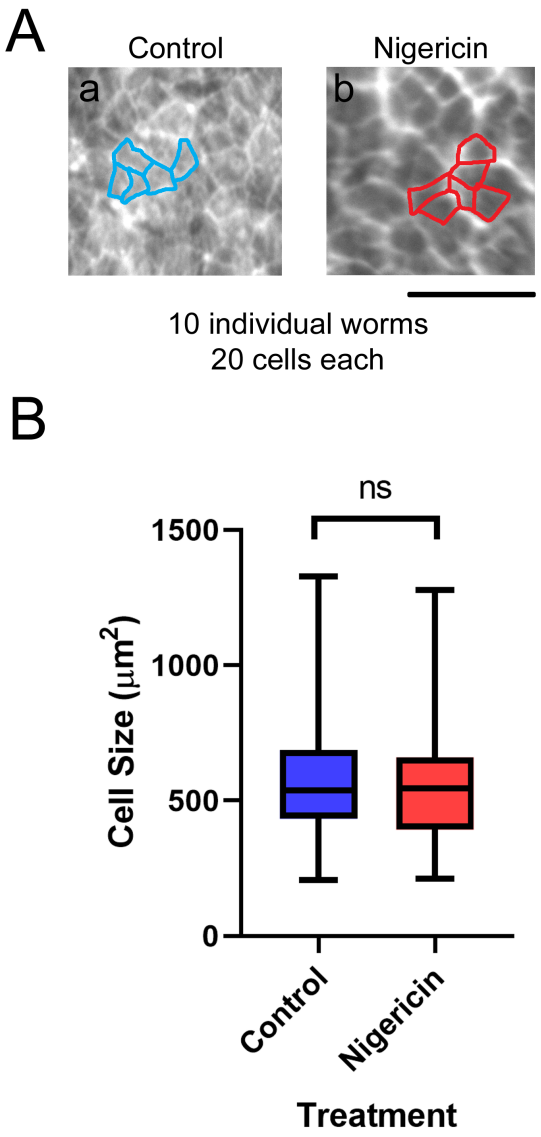

Supplemental Figure 3. Control of cell size after nigericin treatment. (A) Cell membranes stained with SS44 dye and epidermal cells imaged on the dorsal side of the animal in fragments treated with (a) control solution and (b) nigericin solution, showing a few example outlines traced (20 cells per animal in 10 animals were measured for the quantification). (B) Quantification of the cell sizes measured in the control and nigericin-treated fragments, showing no significant difference in cell size ($p>0.05$, N=200, unpaired t-test). Scale bar represents 50 μM.

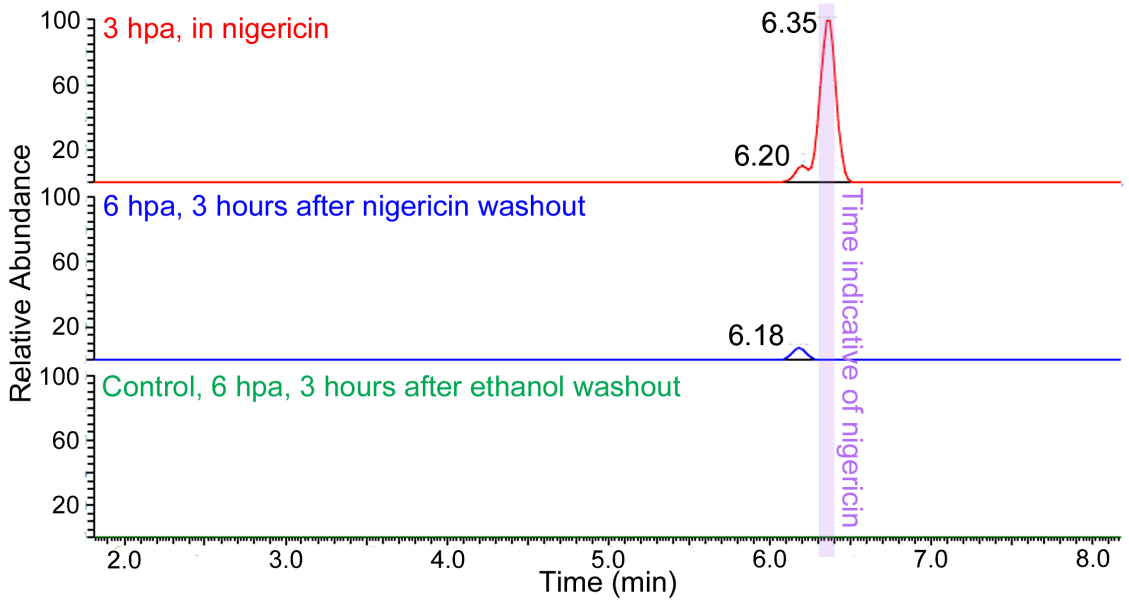

Supplemental Figure 4. Washout of the ionophore. (A) Liquid chromatography mass spectrometry indicating the presence of nigericin. Peak at 6.35 min indicates presence nigericin (lavender region). Peak is clearly defined in animals soaking in nigericin solution at 3 hours post-amputation (red). By 6 hours post-amputation (3 hours post washout) nigericin is no longer present (blue) similar to corresponding 3 hour (brown) and 6 hour (green) corresponding ethanol controls. Peaks seen at 6.20 and 6.18 minutes are other compounds having ions in a similar m/z range. These signals are low and can be considered noise.

As ΔV depends sensitively on the extent to which the fragment polarization profile is amplified by the wound Ca^{2+} response toward the V_{mem} profile of the intact animal as discussed above, the predicted Head - Tail branching ratios also depend on this parameter, as illustrated by the example results shown below (all calculations were performed using the model implementation available at https://chrisfieldsresearch.com/bcar-model.htm). A full-trunk fragment has an anterior cut much closer to the head that the PT fragments used in the experiments reported here; hence it requires less amplification to return to the intact-animal V_{mem} profile.

Supplementary Table 1: Example model results showing nonlinear dependence of Head - Tail branching ratio as a function of amputation-fragment polarization amplification for a full trunk fragment (anterior cut at 20% of animal length, posterior cut at 80% of animal length) with all other model parameters at default values.

Polarization Amplification [%]	Anterior Wound		Posterior Wound	
	Heads [%]	Tails [%]	Heads [%]	Tails [%]
10	20	80	0	100
20	39	61	0	100
30	66	34	0	100
40	90	10	0	100
50	100	0	0	100
…				
100	100	0	1	99

Supplementary Table 2: Example model results showing nonlinear dependence of Head - Tail branching ratio as a function of amputation-fragment polarization amplification for a PT trunk fragment as employed in the experiments reported here (anterior cut at 60% of animal length, posterior cut at 80% of animal length) with all model parameters at default values.

Polarization Amplification [%]	Anterior Wound		Posterior Wound	
	Heads [%]	Tails [%]	Heads [%]	Tails [%]
10	0	100	0	100
20	0	100	0	100
30	0	100	0	100
40	1	99	0	100
50	2	98	0	100
60	6	94	0	100
70	35	65	0	100
80	98	2	0	100
90	100	0	1	99
100	100	0	1	99